

# Non-Gaussianity of diffuse Galactic synchrotron emission at 408 MHz

Sandeep Rana,<sup>1\*</sup> Tuhin Ghosh<sup>2†</sup>, Jasjeet S. Bagla<sup>1‡</sup>, Pravabati Chingangbam<sup>3§</sup>

<sup>1</sup>Indian Institute of Science Education & Research, Mohali, Knowledge city, Sector 81, S.A.S. Nagar, Manauli, Punjab 140306, India

<sup>2</sup>School of Physical Sciences, National Institute of Science Education and Research, HBNI, Jatni 752050, Odissa, India

<sup>3</sup>Indian Institute of Astrophysics, Koramangala II Block, Bangalore 560034, India

Accepted . Received ; in original form

## ABSTRACT

Diffuse Galactic emission at low frequencies is a major contaminant for studies of redshifted 21 cm line studies. Removal of these foregrounds is essential for exploiting the signal from neutral hydrogen at high redshifts. Analysis of foregrounds and its characteristics is thus of utmost importance. It is customary to test efficacy of foreground removal techniques using simulated foregrounds. Most simulations assume that the distribution of the foreground signal is a Gaussian random field. In this work we test this assumption by computing the binned bispectrum for the all-sky 408 MHz map. This is done by applying different brightness temperature ( $T$ ) thresholds in order to assess whether the cooler parts of the sky have different characteristics. We find that regions with a low brightness temperature  $T < 25$  K indeed have smaller departures from a Gaussian distribution. Therefore, these regions of the sky are ideal for future HI intensity mapping surveys.

**Key words:** surveys; cosmology; diffuse radiation, cosmic background radiation, observations

## 1 INTRODUCTION

Diffuse Galactic emission at low frequencies is of immense interest on many counts. These emissions allow us to study the interstellar medium in the Galaxy in unprecedented detail. However, for astronomers interested in radiation from galaxies at high redshifts, radiation from the interstellar medium of the Galaxy is a contaminant. Further, we find that this component is brighter than the radiation from high redshift sources by several orders of magnitude (Furlanetto et al. 2006). The nature of radiation from high redshift sources is very different from the continuum radiation from the interstellar medium. This difference in the spectral properties helps in delineating the radiation from two different sources. The methods deployed in such cases can be categorised in three classes:

- Foreground avoidance (Datta et al. 2010; Pober et al. 2013)
- Foreground removal (Morales et al. 2006; Harker et al. 2009)
- Foreground suppression (Choudhuri et al. 2016; Trott et al. 2016).

All approaches to disentangling signal of interest from foregrounds depends on our understanding of the nature of foregrounds. Therefore understanding and characterising Galactic foregrounds are

critical aspects of designing next generation radio surveys especially HI intensity mapping experiments for the epoch of reionisation (EoR) as well as post-reionisation distribution of HI, such as Murchison Wide Field Array (MWA, Tingay et al. 2013), Low-Frequency Array (LOFAR, van Haarlem et al. 2013), Ooty Wide Field Array (OWFA, Subrahmanya et al. 2017).

The Galactic foregrounds consist of many components with the dominant source at low frequencies being the Galactic diffuse synchrotron emission. At higher frequencies, the free-free emission and dust also contribute significantly and are relevant for studies of the Cosmic Microwave Background radiation (CMB).

Various investigations to understand the Galactic foregrounds for CMB and HI intensity mapping experiments have laid down the generic assumptions. Using inputs from these, we can model spatial and frequency variation of Galactic foregrounds in simulations (Wang et al. 2006; Liu & Tegmark 2012; Jélic et al. 2008, 2010; Santos et al. 2005; Waelkens, A. et al. 2009). The majority of these models use a power-law spectrum with a slowly varying index and an amplitude as free parameters. These Galactic foreground sky simulations assume that parameters of model are approximated by Gaussian random field (GRF), e.g. see Jélic et al. (2008); Tegmark et al. (2000); Santos et al. (2005); Shaw et al. (2015). In this work we analyse the observed emission to test the validity of the assumption of the angular distribution being close to a Gaussian random field. This is done for different subsets of the data where the subsets are defined using the brightness temperature.

While it has been proposed that foregrounds are limited to

\* sandeep@iisermohali.ac.in

† tghosh@niser.ac.in

‡ jasjeet@iisermohali.ac.in

§ prava@iiap.res.in

the wedge in Fourier space, it has been found that there is some leakage beyond the wedge due to spectral variation in foregrounds, especially at small wave numbers (Pober et al. 2013). Further, most foreground removal schemes (Morales et al. 2006; Liu et al. 2009; Harker et al. 2009) assume that foregrounds vary smoothly in frequency and hence can be modelled by a simple function. However, observations suggest (Ghosh et al. 2012) that the spectral response may be fairly non-trivial. Simulation studies for LOFAR (Chapman et al. 2016) where they test foreground removal techniques find that foreground avoidance and removal methods work correctly in case of smooth foregrounds, but failed in case of small wiggles in foreground amplitude with frequency. Thus there is a strong possibility of residuals from foreground subtraction introducing higher moments in spatial variation, especially if foregrounds are non-Gaussian. Thus it is very useful to know if foregrounds have significant non-Gaussian features. The HI-signal itself is expected to be slightly non-Gaussian due to non-linear aspects of gravitational clustering (Bharadwaj & Pandey 2005). Cooray (2005) proposed a foreground removal technique where the prior knowledge of non-Gaussian structure of foregrounds can be combined with its frequency information to separate out HI fluctuations from the foregrounds.

A number of methods for quantifying departure from Gaussianity have been suggested, e.g., Kullback-Leibler divergence (see Ben-David et al. 2015a), higher order moments (skewness, kurtosis) (Ben-David et al. 2015b; Contaldi et al. 2000; Munshi et al. 2013), and three-point correlation function (Chen & Szapudi 2005). One of the tools for analysing the statistical properties of smooth random fields are the Minkowski Functionals (Adler 1981; Tomita 1986). They are quantities that characterise the geometrical and topological properties of excursion sets of random fields. They contain correlations of arbitrary order and hence are very useful for searches for non-Gaussianity in observed cosmological data. They were first applied to cosmological fields, particularly the CMB (Gott et al. 1990; Mecke et al. 1994; Schmalzing & Buchert 1997; Schmalzing & Gorski 1998). They have been extensively used to constrain primordial non-Gaussianity in the CMB data (Novikov et al. 2000; Komatsu et al. 2011; Planck Collaboration et al. 2016; Buchert et al. 2017). They have also been used to detect the presence of residual foreground contamination in cleaned CMB data (Chingangbam & Park 2013) and to study the effect of lensing on CMB fields (Munshi et al. 2016).

Ben-David et al. (2015b) using the all-sky renewed version of Haslam 408 MHz map (Remazeilles et al. 2015) reported that a patch of  $3^\circ.7 \times 3^\circ.7$  at higher Galactic latitudes could be well approximated by GRF (see Figs. 4 and 5 of Ben-David et al. 2015b). However their results are more localised as they have obtained local skewness and kurtosis for specific patches in the sky. In contrast to their approach, we are using the binned bispectrum estimator (Bucher et al. 2010, 2016) to test the validity of the Gaussian approximation. In view of the large area surveys envisaged by Square Kilometre Array (SKA) and its precursors (MWA, LOFAR, and OWFA) we do not limit ourselves to a small patch and we work with different sky brightness thresholds.

Bispectrum estimation is a well studied topic in views of several attempts to search for primordial non-Gaussianity in the CMB (Gangui & Martin 2000; Komatsu & Spergel 2001; Bucher et al. 2010; Fergusson et al. 2012; Casaponsa et al. 2013). Non-Gaussianity can also arise due to the Sachs-Wolfe effect, gravitational lensing, reionisation, etc. (Mangilli & Verde 2009; Lewis et al. 2011; Serra & Cooray 2008; Munshi et al. 2014). For present work, we use the all-sky 408 MHz map (Remazeilles et al. 2015)

and binned bispectrum estimator (Bucher et al. 2010, 2016) to quantify non-Gaussian nature of the Galactic foregrounds. In Sect. §2, we discuss simulations of Galactic foregrounds, formalism for binned bispectrum estimator. In Sect. §3 we discuss the analysis and results of bispectrum analysis. The Minkowski functional analysis is presented in Sect. §4. Summary and discussions are presented in Sect. §5.

## 2 FORMALISM

The low-frequency Galactic foregrounds consists of three components - diffuse synchrotron emission, diffuse free-free emission from ionised gas and emission from point sources, which mainly include stellar remnants. At low frequencies the free-free is weakest among the three components but still a dominant component as compared to cosmological signal (see Fig. 5 of Santos et al. 2005). However at higher frequencies ( $\geq 50$  GHz) free-free becomes a dominant foreground along with thermal dust.

The intensity of the diffuse Galactic synchrotron emission is expressed in terms of its angular power spectrum ( $C_\ell$ ) where  $C_\ell \propto \ell^\alpha \nu^{2\beta}$ . Here  $\alpha$  corresponds to the variation of the power spectra as a function of angular separation on the sky and  $\beta$  corresponds to the variation in frequency (Tegmark et al. 2000; Giardino et al. 2002; De Oliveira-Costa et al. 2008; Liu & Tegmark 2012).

To simulate the effect of Galactic foreground one assumes a power-law form with indices  $\alpha$  and  $\beta$ . For low-frequency cosmological observations, the Haslam map at 408 MHz acts as standard template for studying diffuse Galactic foregrounds (Haslam et al. 1982; Remazeilles et al. 2015). The spectral index varies in the range  $\alpha = -2.5$  to  $-3.0$  down to a degree angular scale at 408 MHz (Tegmark et al. 2000; De Oliveira-Costa et al. 2008).

Tegmark et al. (2000) report frequency spectrum varying as  $\beta \sim -2.8$  with  $\Delta\beta \sim 0.15$ , that is the variation in frequency spectral index arises due to variation along different line of sights. Studies of low-frequency foregrounds in the frequency range 100–200 MHz find standard deviation in  $\beta$  to be approx 0.1 (Shaver et al. 1999). This has also been studied elsewhere, e.g., see Rogers & Bowman (2008); Ali et al. (2008); Ghosh et al. (2012); Pen et al. (2009). In contrast to earlier approach, Jélic et al. (2008) use to simulate  $T$  in four-dimensional accounting for the variation of foregrounds along the line of sight ( $z$  coordinate):

$$T(x, y, \nu) = C \int A(x, y, z, \nu) dz, \quad (1)$$

where  $C$  is the normalisation constant and  $A(x, y, z, \nu)$  is modelled as power-law  $A(x, y, z, \nu) = A(x, y, z, \nu_0) \left(\frac{\nu}{\nu_0}\right)^{\beta(x, y, z)}$ .

Several simulation studies of foregrounds have been carried out (Jélic et al. 2008, 2010; Santos et al. 2005; Waelkens, A. et al. 2009). Some of these encompass a broad range of frequencies while others are more specialised for a specific application. Most of these simulations model intensity and power-law index of the diffuse synchrotron emission as GRFs.

For example, the publicly available *Hammurabi* code, simulates all-sky maps of the polarised synchrotron emission, free-free emission and ultra-high energy cosmic ray at all frequencies in a three-dimensional (3D) HEALPIX grid format (Waelkens, A. et al. 2009). It assumes a 3D model of the Galactic magnetic field, cosmic ray electron density and thermal density distribution, for the detailed description see Waelkens, A. et al. (2009). The turbulent component of the magnetic field is simulated as a Gaussian random-field realisation given a magnetic-field power spectrum.

The realistic turbulent field is not Gaussian, therefore the simulations fail to reproduce the higher order statistics of the data. The LOFAR EOR simulation pipeline (Jélic et al. 2008, 2010) also assumes that both  $A(x, y, z, \nu)$  and the power-law index  $\beta(x, y, z, \nu)$  of diffuse Galactic synchrotron emission as a GRFs.

The aim of the present study is to evaluate the validity of the use of GRFs to represent the 408 MHz brightness temperature fluctuations on the sky. We do this by computing the magnitude of departure of the observed spatial distribution from a Gaussian distribution. Of course, projection effects in models that take spatial distributions in 3D may introduce departures from the Gaussian distribution.

In the present analysis, we are only considering synchrotron intensity map and will not comment on the polarisation of diffuse synchrotron emission as this is beyond the scope of this work. We quantify non-Gaussianity of the diffuse synchrotron emission by computing the three-point correlation function in harmonic space as a function of sky brightness.

## 2.1 Binned bispectrum estimator

Bispectrum estimation is a popular approach for quantifying non-Gaussianity (Gangui & Martin 2000; Komatsu & Spergel 2001; Santos et al. 2003; Komatsu et al. 2005; Fergusson et al. 2012). It is particularly used for non-Gaussianity studies of CMB anisotropies in temperature and polarisation (Planck Collaboration et al. 2016).

Given a distribution of brightness temperature  $T$  over all-sky, one can decompose it into spherical harmonic basis with amplitudes  $a_{\ell m}$

$$T(\Omega) = \sum_{\ell, m} a_{\ell m} Y_{\ell m}(\Omega). \quad (2)$$

We can compute amplitudes  $a_{\ell m}$  from the temperature distribution on the sky as

$$a_{\ell m} = \int T(\Omega) Y_{\ell m}^*(\Omega) d\Omega. \quad (3)$$

The angle-averaged angular bispectrum is defined as

$$B_{\ell_1 \ell_2 \ell_3} = N \sum_{m_1, m_2, m_3} \begin{pmatrix} \ell_1 & \ell_2 & \ell_3 \\ m_1 & m_2 & m_3 \end{pmatrix} a_{\ell_1 m_1} a_{\ell_2 m_2} a_{\ell_3 m_3} \quad (4)$$

where

$$N = \frac{(2\ell_1 + 1)(2\ell_2 + 1)(2\ell_3 + 1)}{4\pi} \begin{pmatrix} \ell_1 & \ell_2 & \ell_3 \\ 0 & 0 & 0 \end{pmatrix}^2 \quad (5)$$

is the number of possible triangles of side  $(\ell_1, \ell_2, \ell_3)$  on a sphere (see Rotenberg et al. 1959). The angle-average bispectrum  $B_{\ell_1 \ell_2 \ell_3}$  is pairwise symmetric in  $(\ell_1, \ell_2, \ell_3)$ . Therefore in our analysis we only consider the subspace  $\ell_1 \leq \ell_2 \leq \ell_3$ . The presence of Wigner  $3j$  symbol imposes condition that  $B_{\ell_1 \ell_2 \ell_3} \neq 0$  only for  $m_1 + m_2 + m_3 = 0$  and  $|\ell_1 - \ell_2| \leq \ell_3 \leq \ell_1 + \ell_2$ . Additional selection condition  $\ell_1 + \ell_2 + \ell_3 = \text{even}$  comes due to presence of the Wigner  $3j$  symbol when all  $m$  values are zero (see Gangui & Martin 2000; Komatsu & Spergel 2001), which means that only even parity modes are considered.

The binned bispectrum introduced by Bucher et al. (2010) is defined in terms of maximally filtered brightness temperature as

$$b_{i_1 i_2 i_3} = \frac{1}{C_{i_1 i_2 i_3}} \int d\Omega T_{i_1}(\Omega) T_{i_2}(\Omega) T_{i_3}(\Omega), \quad (6)$$

where

$$T_i(\Omega) = \sum_{\ell, m} f_{\ell}^{i_1} a_{\ell m} Y_{\ell m}(\Omega). \quad (7)$$

$C_{i_1 i_2 i_3}$  is the number of valid  $\ell$  triplets within  $(i_1, i_2, i_3)$  and  $f_{\ell}$  is a filter function in harmonic space. The binned bispectrum estimator is optimised by working with  $T_i$ , where each value of  $i$  refers to a range of  $\ell$  values. This scheme of working with bins is described in detail by Bucher et al. (2010). The advantage of using binned bispectrum estimator is that it is computationally faster than the angle-averaged bispectrum estimator. The binned bispectrum  $b_{i_1 i_2 i_3}$  is related to angle-averaged bispectrum by the relation

$$b_{i_1 i_2 i_3} = \sum_{\ell_1 \ell_2 \ell_3} f_{\ell_1}^{i_1} f_{\ell_2}^{i_2} f_{\ell_3}^{i_3} \frac{B_{\ell_1 \ell_2 \ell_3}}{\sqrt{N}}. \quad (8)$$

Binned bispectrum, by construction, includes both odd and even parity modes, and there is no ab initio reason for giving preference to specific parity mode in case of the diffused Galactic synchrotron emission. Therefore in our analysis we include both parity modes.

In presence of partial sky coverage and a finite beam resolution of a given map, the binned bispectrum estimator defined in Eq. 6 needs to be debiased. The linear order correction term is written as (Bucher et al. 2016)

$$b_{i_1 i_2 i_3}^{\text{lin}} = \frac{1}{C_{i_1 i_2 i_3}} \int d\Omega \left[ T_{i_1} \langle T_{i_2}^G T_{i_3}^G \rangle + T_{i_2} \langle T_{i_1}^G T_{i_3}^G \rangle + T_{i_3} \langle T_{i_1}^G T_{i_2}^G \rangle \right]. \quad (9)$$

Here the term inside angular brackets is an average over 1000 Gaussian realisations which have the same underlying power spectrum as the observed data. We discuss this in detail in the next section.

## 3 ANALYSIS

### 3.1 Masking

To investigate the non-Gaussian nature of diffuse synchrotron emission, we use a renewed version of all-sky 408MHz map, which is further de-sourced and de-striped to remove any remaining point source contamination that was present in original Haslam map (Remazeilles et al. 2015).

Taking this as a reference map, we apply sky brightness thresholds to take out prominent non-Gaussian Galactic structures. We have used the publicly available `Healpy`<sup>1</sup> package, the python version of `HEALPIX`<sup>2</sup> (Górski et al. 2005), and employ the following steps:

- First, we degrade 408 MHz map from  $N_{\text{side}} = 512$  to 128 since the resolution of processed 408 MHz map is  $56'$  (Remazeilles et al. 2015). We then apply a Galactic cut ( $|b| < 10^\circ$ ) to take out contamination from the Galactic plane.
- We mask bright Loop-I ring, which comes from an old supernova remnant. The mask region includes  $\pm 4^\circ$  width cut around a circle of radius  $58^\circ$  entered at  $(l, b) = (329^\circ, 17^\circ 5')$ .
- We construct four sky masks by applying brightness temperature thresholds of 25, 30, 40, and 60 K.

To avoid leakage of power due to sharp cutoff between the masked and the unmasked region, we apodized the masks by convolving with a  $5^\circ$  FWHM Gaussian. Such a smooth Gaussian filter

<sup>1</sup> <https://pypi.python.org/packages/source/h/healpy/healpy-1.7.4.tar.gz>

<sup>2</sup> <http://healpix.sourceforge.net>

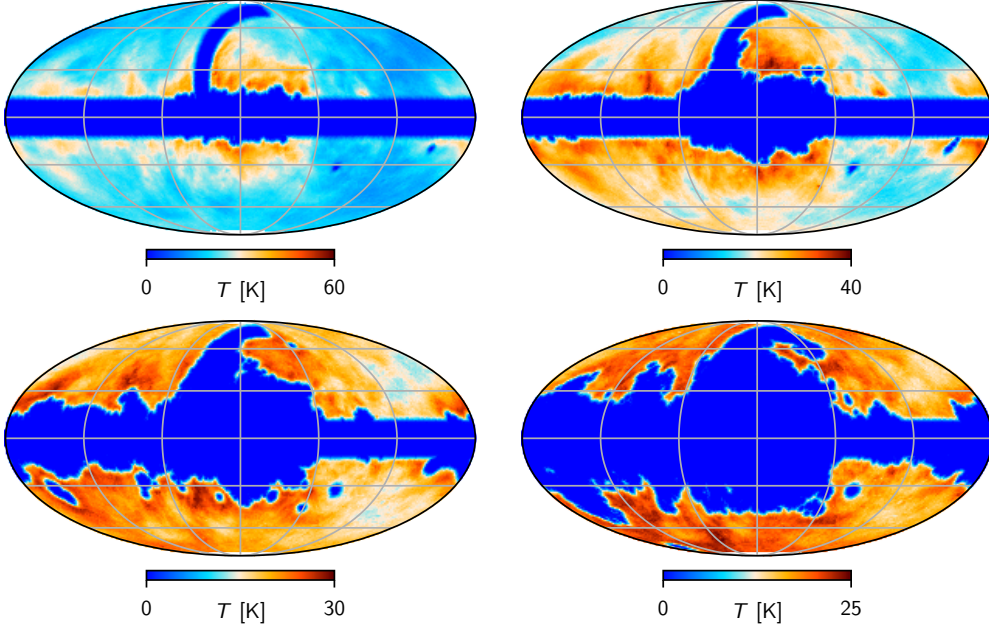


**Figure 1.** 408 MHz map multiplied by a  $5^\circ$  FWHM Gaussian apodized masks at different sky brightness thresholds as described in Sect. 3.1. Here temperature scales are different for each map to show brightness temperature variation. The effective fractional sky coverages,  $f_{\text{sky}}$ , are 0.74 ( $T < 60$  K), 0.63 ( $T < 40$  K), 0.56 ( $T < 30$  K), and 0.41 ( $T < 25$  K) respectively.

function reduces the leakage of the signal towards the edges of the unmasked region. Figure 1 shows the 408 MHz map multiplied by the apodized masks at different sky brightness thresholds. The effective fractional sky coverages,  $f_{\text{sky}}$ , are 0.74 ( $T < 60$  K), 0.63 ( $T < 40$  K), 0.56 ( $T < 30$  K), and 0.41 ( $T < 25$  K).

### 3.2 Bispectrum estimation

After apodization of masks, we use `PolSpice`<sup>3</sup> routine (Chon et al. 2004) to compute the full-sky  $TT$  power spectra at different sky brightness. The `PolSpice` routine corrects for the sky mask, beam smoothing and pixel window function. The correction for incomplete sky coverage is performed by first estimating the correlation function in pixel space. As 408 MHz map is non-Gaussian and anisotropic, all the statistical properties of the Galactic synchrotron emission might not be captured by the power spectrum analysis. For further analysis, we take each of the four  $TT$  power spectrum and simulate 1000 Gaussian sky realisations using `Healpy` facility `synfast` and apply the Gaussian beam of FWHM  $56'$ . We compare the two-point statistics of the data and the Gaussian simulations for multipole range where they are reliably estimated. The lower bound on  $\ell$  value comes from the masking of the sky region. The resolution of the 408 MHz map puts the bound on high  $\ell$  mode. Therefore for the power spectrum and bispectrum analyses, we only consider the  $\ell$ -range  $\in [10, 180]$ .

We consider a simple linear binning scheme and divide the available  $\ell$  range into  $N_{\text{bin}} = 11$ , where  $N_{\text{bin}}$  is the total number

of bins. The binning scheme is defined as follows:

$$f_\ell^i = \begin{cases} \cos^2\left(\frac{\pi}{2} \times \frac{\ell_0^i - \ell}{\Delta\ell}\right) & \text{for } \ell_0^i - \Delta\ell \leq \ell < \ell_0^i \\ 1 & \text{for } \ell_0^i \leq \ell \leq \ell_1^i \\ \cos^2\left(\frac{\pi}{2} \times \frac{\ell - \ell_1^i}{\Delta\ell}\right) & \text{for } \ell_1^i < \ell \leq \ell_1^i + \Delta\ell, \end{cases} \quad (10)$$

where  $\ell_0^i$  and  $\ell_1^i$  are the first and the last  $\ell$  values of a given  $i$  bin and  $\Delta\ell = 5$ . Table 1 summarises the binning scheme that we employ in our analysis. The filter function is defined in such a way that  $\sum_i (f_\ell^i)^2 = 1$  for all bins, except for the first and last bins. It has been shown that the variance of the binned bispectrum changes with the binning scheme. Therefore, one has to optimise the binning scheme to obtain the minimum variance binned bispectrum estimator (Bucher et al. 2010; Casaponsa et al. 2013; Bucher et al. 2016). In the present analysis, we only consider one binning scheme. We have checked that the final results of the paper does not depend on the binning scheme.

Once the binning scheme and  $\ell$ -range are defined, we then calculate  $D_\ell = \ell(\ell + 1)C_\ell/2\pi$  in each  $\ell$  bin for all 1000 Gaussian realisations and evaluate the ensemble mean and standard deviation value of  $D_\ell$ . Similarly, we obtain  $D_\ell$  in each  $\ell$  bin for the real data. In Fig. 2 we plot both averaged and actual binned  $D_\ell$ , and both of them agree well within  $1\sigma$  and ensures that simulated maps are in good agreement with actual masked 408 MHz map as far as the power spectrum is concerned.

As a first step of bispectrum estimation, we create binned filtered maps as given by Eq. (7) in each  $i$  bin. Upon close inspection of these filtered maps, we have realised that the bright Galactic synchrotron emission from the Galactic plane leaks into the high latitude sky. To avoid this problem, we first mask the all-sky 408 MHz map with a sky brightness threshold of 80 K and then compute the binned filtered maps. With 80 K threshold, we only take out the brightest part of the synchrotron emission close to the Galactic plane. We then apply the four binary masks to the filtered 408 MHz

<sup>3</sup> <http://www2.iap.fr/users/hivon/software/PolSpice/index.html>

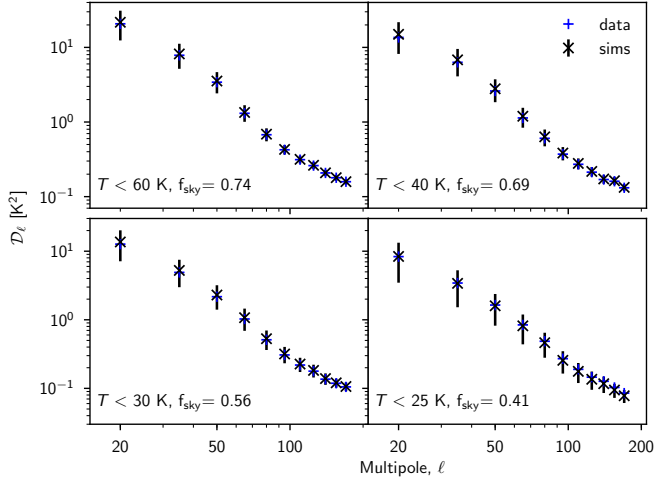


**Figure 2.** Binned angular power spectrum as a function of multipoles for different sky brightness thresholds, blue circles is for real data and black open circles is a mean of 1000 Gaussian realisations. The data agrees with the Gaussian realisations within  $1\sigma$  confidence limit.

maps. The same procedure is applied to the 1000 Gaussian sky realisations for each sky brightness threshold.

The numerical implementation of the unbiased binned bispectrum estimator is

$$b_{i_1 i_2 i_3}^o = \frac{1}{C_{i_1 i_2 i_3}} \sum_{j=1}^{N_{\text{pix}}} \frac{M_j}{4\pi N_{\text{pix}}} (T_j^{i_1} T_j^{i_2} T_j^{i_3} - T_j^{i_1} \langle T_j^{i_2} T_j^{i_3} \rangle + T_j^{i_2} \langle T_j^{i_1} T_j^{i_3} \rangle + T_j^{i_3} \langle T_j^{i_1} T_j^{i_2} \rangle), \quad (11)$$

where  $M$  is the binary mask applied binned filtered maps,  $N_{\text{pix}} = \sum_j M_j$  is the fraction of sky available,  $C_{i_1 i_2 i_3}$  is the number of valid triplets within the bin  $i_1 i_2 i_3$ . If there is no valid triplet in  $(i_1, i_2, i_3)$  bins, we put  $C_{i_1 i_2 i_3} = 0$  and ignore the contribution to binned bispectrum. We apply the above estimator to obtained binned bispectrum value for the four sky masks. Similarly, we repeat the same procedure on 1000 Gaussian sky realisations that have the same underlying power spectrum as the observed 408 MHz map. From the simulations, we obtain the ensemble mean and  $1\sigma$  standard deviation of the binned bispectrum value as a function of sky brightness.

### 3.3 Bispectrum visualisation

To establish the statistical significance of the observed binned bispectrum of 408 MHz map as a function of sky brightness thresholds, we compute the deviation,  $\Delta = (b_{i_1 i_2 i_3}^o - \langle b_{i_1 i_2 i_3}^G \rangle) / \sigma_{i_1 i_2 i_3}^G$ , between the data and the ensemble mean of large set of 1000 Gaussian simulations with the same underlying angular power spectrum as the 408 MHz map. The  $1\sigma$  standard deviation of 1000 Gaussian simulations binned bispectrum is denoted by the index  $\sigma_{i_1 i_2 i_3}$ . Unlike the primordial non-Gaussianity study of CMB, we do not have a standard bispectrum template to compute local non-linear coupling parameter ( $f_{\text{NL}}$ ).

Figures 3, 4, 5 and 6 show the two-dimensional plot of  $\Delta$  in  $\ell_1 - \ell_2$  plane fixing  $\ell_3$  parameter. The plots are symmetric about the diagonal in  $\ell_1 - \ell_2$  plane because of the symmetric nature of  $b_{i_1 i_2 i_3}^o$  under the permutation of  $\ell$  pairs.

Similarly in Fig. 7, we plot  $\ell_3 \in [55, 75]$  for different sky

**Table 1.**  $\ell$  range corresponding to  $i$  bin

| bin      | $\ell_{\min}$ | $\ell_{\max}$ | $\ell_0$ | $\ell_1$ |
|----------|---------------|---------------|----------|----------|
| $i_1$    | 10            | 30            | 15       | 25       |
| $i_2$    | 25            | 45            | 30       | 40       |
| $i_3$    | 40            | 60            | 45       | 55       |
| $i_4$    | 55            | 75            | 60       | 70       |
| $i_5$    | 70            | 90            | 75       | 85       |
| $i_6$    | 85            | 105           | 90       | 100      |
| $i_7$    | 100           | 120           | 105      | 115      |
| $i_8$    | 115           | 135           | 120      | 130      |
| $i_9$    | 130           | 150           | 135      | 145      |
| $i_{10}$ | 145           | 165           | 150      | 160      |
| $i_{11}$ | 160           | 180           | 165      | 175      |

brightness thresholds. One can see a clear decreasing trend in bispectrum signal as we go from 60 K maps to 25 K thresholds on all angular scales. Table 2 shows the  $(i_1, i_2, i_3)$  bin triplets where the absolute value of the bispectrum signal of 408 MHz map deviate more than  $4\sigma$  with respect to ensemble mean of 1000 Gaussian realisations. As indicated in Table 2 and Fig. 6 that in case of 25 K sky brightness threshold, the real data is consistent within  $3\sigma$  deviation with respect to Gaussian simulations at  $\ell \geq 60$ . At large angular scales,  $\ell < 60$ , the deviation of the real data varies between 4 and  $9\sigma$  with respect to the Gaussian simulations. We also compute the skewness and kurtosis of the real and imaginary part of  $a_{\ell m}$  distribution in  $i$  bins for sky brightness threshold maps and corresponding 1000 Gaussian simulations. We report that both skewness and kurtosis for actual data is in agreement with the Gaussian simulations well within  $2\sigma$ . However, Pietrobon et al. (2009) show that unlike bispectrum the skewness of  $a_{\ell m}$  distribution is sensitive only to a specific type of triangle configuration and does not represent the overall picture as far as non-Gaussian features are concerned (see Appendix A).

## 4 MINKOWSKI FUNCTIONALS

In CMB studies, the scalar Minkowski Functionals (MFs hereafter) is widely used to measure the non-Gaussianity (Ducoat et al. 2013). Unlike binned bispectrum estimator, MFs are defined in the pixel space. MFs are sensitive to the contribution of higher order correlations, where binned bispectrum estimator is only sensitive to three-point correlation function. We employ MFs estimator to cross validate our findings for bispectrum in case of 408 MHz map.

### 4.1 Method

The Minkowski Functionals are a class of morphological descriptors for structures in  $d$ -dimensional space. In two dimensions each level or excursion set of a smooth random field at a chosen threshold value typically consists of two kinds of structures, namely, connected regions and holes within the connected regions. The morphological properties of these structures vary smoothly with the threshold value. The functional form of these variations can reveal the statistical nature of the field. For our purpose in this paper we focus on fields defined on the sphere,  $\mathcal{S}^2$ .

Let  $f$  denote a generic random field with its mean and rms denoted by  $\mu$  and  $\sigma_0$ , respectively. We define  $u$  to be the standard

**Table 2.** Triplet bins for which  $|\Delta| > 4$  where,  $\Delta = (b_{i_1 i_2 i_3}^o - \langle b_{i_1 i_2 i_3}^G \rangle) / \sigma_{i_1 i_2 i_3}^G$ 

| $T < 60$ K |            |             |            |            |             |            |            |            |             |            |
|------------|------------|-------------|------------|------------|-------------|------------|------------|------------|-------------|------------|
| (1, 1, 6)  | (1, 1, 7)  | (1, 1, 9)   | (1, 2, 3)  | (1, 2, 7)  | (1, 2, 8)   | (1, 3, 4)  | (1, 3, 8)  | (1, 4, 5)  | (1, 4, 10)  | (1, 5, 10) |
| (1, 6, 7)  | (1, 6, 11) | (1, 7, 8)   | (1, 8, 9)  | (1, 9, 10) | (2, 2, 4)   | (2, 3, 9)  | (2, 3, 10) | (2, 4, 11) | (2, 5, 7)   | (2, 5, 10) |
| (2, 5, 11) | (2, 6, 11) | (2, 8, 10)  | (3, 4, 11) | (3, 7, 10) | (3, 8, 11)  | (4, 6, 10) | (4, 7, 10) | (4, 7, 11) | (5, 5, 5)   | (5, 5, 10) |
| (5, 6, 10) | (5, 6, 11) | (5, 10, 10) | (6, 6, 11) | (7, 7, 10) | (7, 8, 9)   | (7, 9, 11) |            |            |             |            |
| $T < 40$ K |            |             |            |            |             |            |            |            |             |            |
| (1, 1, 2)  | (1, 1, 7)  | (1, 2, 3)   | (1, 2, 7)  | (1, 3, 4)  | (1, 3, 9)   | (1, 3, 10) | (1, 4, 8)  | (1, 4, 10) | (1, 4, 11)  | (1, 5, 6)  |
| (1, 5, 11) | (1, 6, 11) | (1, 7, 8)   | (1, 8, 9)  | (1, 9, 10) | (1, 10, 11) | (2, 2, 4)  | (2, 2, 11) | (2, 3, 9)  | (2, 3, 10)  | (2, 5, 11) |
| (2, 6, 11) | (2, 8, 8)  | (2, 10, 10) | (3, 4, 11) | (3, 6, 9)  | (3, 8, 9)   | (4, 6, 10) | (5, 5, 10) | (5, 6, 11) | (7, 10, 10) |            |
| $T < 30$ K |            |             |            |            |             |            |            |            |             |            |
| (1, 4, 9)  | (1, 5, 10) | (1, 7, 8)   | (1, 8, 10) | (2, 6, 11) | (3, 4, 10)  | (3, 4, 11) | (3, 5, 11) | (3, 8, 9)  | (4, 4, 11)  | (5, 6, 11) |
| $T < 25$ K |            |             |            |            |             |            |            |            |             |            |
| (1, 2, 9)  | (1, 2, 10) | (1, 3, 10)  | (1, 4, 8)  | (1, 5, 7)  | (1, 6, 10)  | (1, 7, 11) | (1, 8, 9)  | (2, 3, 11) | (2, 6, 11)  | (3, 5, 11) |

normal field given by  $u \equiv (f - \mu) / \sigma_0$ . Let  $\nu$  be the threshold value chosen from the range of  $u$ ,  $Q$  be the excursion set indexed by  $\nu$ , and  $\partial Q$  the set of the corresponding boundary contours. Then, the MFs for the structures of the excursion set are defined as follows:

$$V_0(\nu) \equiv \frac{1}{4\pi} \int_Q da, \quad (12)$$

$$V_1(\nu) \equiv \frac{1}{4} \int_{\partial Q} dl, \quad (13)$$

$$V_2(\nu) \equiv \frac{1}{2\pi} \int_{\partial Q} \kappa dl, \quad (14)$$

where  $da$  is the area element of the excursion set,  $dl$  is the line element on  $\partial Q$  and  $\kappa$  is the curvature at each point of the boundary contours. It is clear that  $V_0$  is the area fraction occupied by the excursion set on the sphere whose radius is normalised to one.  $V_1$  is related to the total length of the boundary contours, and  $V_2$  is the number of connected regions minus the number of holes. For an isotropic GRF, analytic expressions for the ensemble expectation values of the MFs have been derived by Tomita (1986). They are:

$$V_0 = \frac{1}{2} \operatorname{erfc} \left( \frac{\nu}{\sqrt{2}} \right), \quad (15)$$

$$V_1 = \frac{1}{8} \left( \frac{\sigma_1}{\sigma_0} \right) e^{-\nu^2/2}, \quad (16)$$

$$V_2 = \frac{1}{2\pi^3} \left( \frac{\sigma_1}{\sigma_0} \right)^2 \nu e^{-\nu^2/2}, \quad (17)$$

where  $\sigma_1 = \sqrt{\langle |\nabla f|^2 \rangle}$  is the rms of the gradient of the field. For a given field whose statistical nature is not known a priori, one can compute the MFs and compare with these analytic expressions to test whether it is Gaussian or has non-Gaussian deviations.

## 4.2 Estimating MFs

In Sects. 3.1 and 3.2, we have outlined our method for constructing brightness temperature threshold masks using 408 MHz map and corresponding 1000 Gaussian sky realisations for the binned bispectrum estimation. To evaluate all the three MFs as a function of angular scales, we apply a low-pass filtering to both actual and simulated data sets.

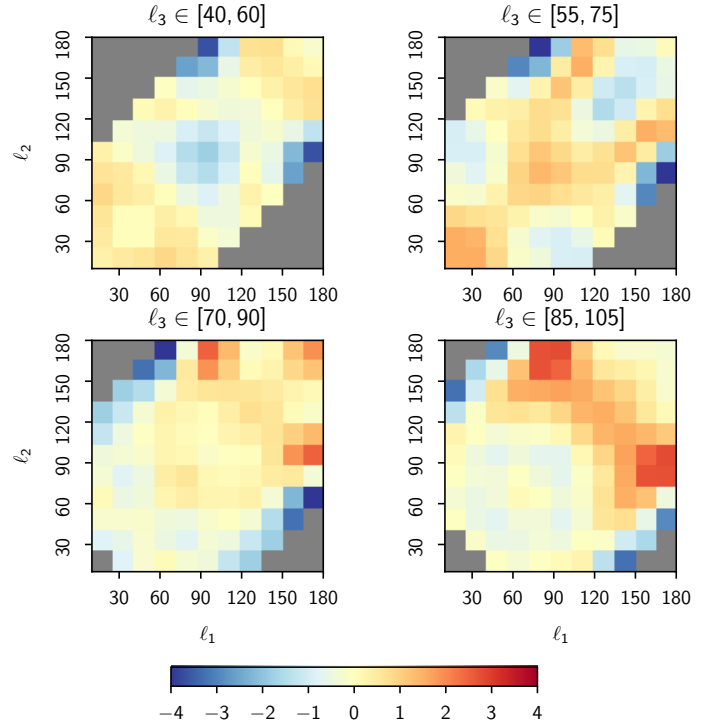


**Figure 3.** Variation of  $\Delta$  in  $\ell_1 - \ell_2$  plane fixing  $\ell_3$  bin range for 408 MHz brightness threshold  $T < 60$  K. The plots are symmetric  $\ell_1 - \ell_2$  plane because of the symmetric nature of  $b_{\ell_1 \ell_2 \ell_3}$  under the permutation of  $\ell$  pairs.

$$f(\ell) = \begin{cases} 0 & \text{for } \ell < \ell_c - \Delta\ell \\ \cos^2 \left( \frac{\pi}{2} \times \frac{(\ell_c - \ell)}{\Delta\ell} \right) & \text{for } \ell_c - \Delta\ell \leq \ell < \ell_c \\ 1 & \text{for } \ell \geq \ell_c. \end{cases} \quad (18)$$

We choose three different values of low  $\ell$  cutoff corresponding to  $\ell_c = 50, 70, \text{ and } 90$ . Our filtering scheme takes care of artefacts arises in the filtered 408 MHz map due to sharp cut-off around the edge of the bin. We checked that the final results is independent of the filtering scheme that we employed in our analysis. As in

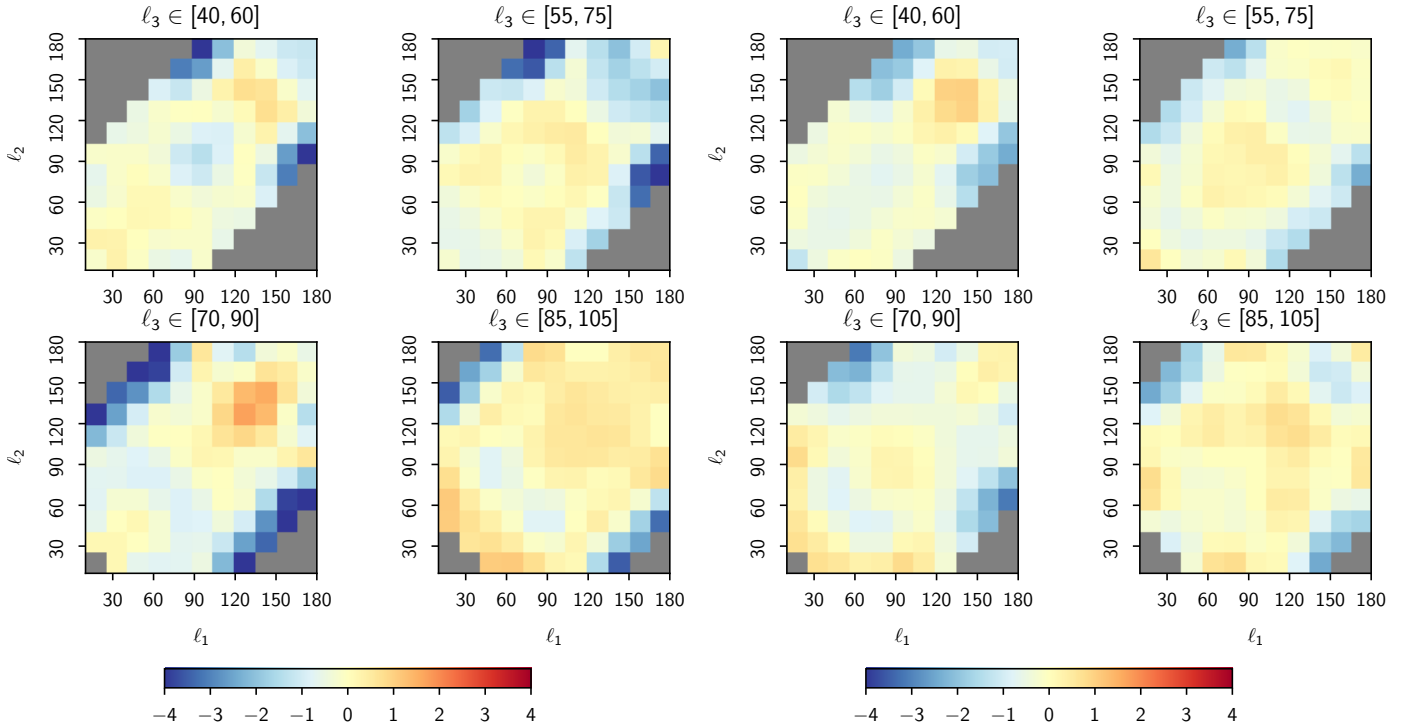


**Figure 4.** Same as Fig. 3, but for 408 MHz brightness threshold  $T < 40$  K.

**Figure 5.** Same as Fig. 3, but for 408 MHz brightness threshold  $T < 30$  K.

Sect. 3.2 to restrain leakage from bright galactic plane in binned filtered maps, we first apply the brightness temperature threshold of 80 K to 408 MHz map.

To compute MFs for an arbitrary field, we employ the method outlined in Schmalzing & Gorski (1998). This method involves expressing Eq. (13) and (14) regarding first and second derivatives of the field, converting the line integrals to area integrals by introducing delta function for the field at the threshold values, and then, integrating over the sphere.

We use the same 1000 random Gaussian realisations for each brightness temperature threshold that we have generated for the binned bispectrum analysis. We compute ensemble mean and  $1\sigma$  standard deviation of three MF for each of the four case. For two extreme sky brightness thresholds  $T < 60$  K and  $T < 25$  K, we plot the three MFs for the real data, and the ensemble mean of 1000 Gaussian realisations as shown in Figs 8 and 9. For 60 K map, the real data and Gaussian simulations differ from each other significantly for all three MFs. Since MFs are sensitive to the entire hierarchy of higher order correlations unlike bispectrum, therefore, we aspect higher deviation ( $3\sigma$  grey shaded regions) between actual data and Gaussian simulation. As in case of bispectrum here also 25 K maps, for multipole cut-off  $\ell_c \geq 60$  ( $\theta < 3^\circ$ ), the real data is relatively consistent with Gaussian simulations.

## 5 SUMMARY AND DISCUSSION

In this article, we discussed three-point statistics of Galactic synchrotron emission at 408 MHz. We used the re-processed version of all-sky 408 MHz map and divide the sky into four regions based on the sky brightness. For each brightness temperature threshold using PolSpice routine, we obtained  $TT$  power spectra which are corrected for the sky mask, beam smoothing and pixel window function and created 1000 Gaussian sky realisations. We applied

binned bispectrum estimator to both the data and Gaussian realisations and obtained bispectrum value in bins of multipole. We have also applied MF estimator to compute three MF values for different multipole cut-off  $\ell_c$ . Our conclusions are as follows:

- Although the all-sky map of 408 MHz sky is highly non-Gaussian, we find that the regions with lower brightness temperature have a smaller bispectrum. For example, bispectrum in 408 MHz map with a threshold at 25 K is small enough to be indistinguishable from the ensemble of Gaussian simulations. For higher sky brightness temperature thresholds ( $T > 40$  K), the data shows clear difference from the Gaussian sky realisations.
- The three MFs for the actual maps deviate significantly from Gaussian realisations for higher brightness temperature thresholds. As we go to lower brightness threshold and higher value of multipole cut-off ( $\ell_c \geq 60$ ), the three MF of the real data agree well the Gaussian simulations within the  $3\sigma$ .
- However, the skewness and kurtosis of  $a_{\ell m}$  distribution of 408 MHz map agree well within  $2\sigma$  with respect to Gaussian realisations for all sky brightness temperature thresholds. Since skewness of  $a_{\ell m}$  distribution corresponds to a equilateral configuration (Pietrobon et al. 2009), therefore it does not capture non-Gaussian features arising from other triangular configurations to which binned bispectrum estimator is sensitive.

Our results indicate scales of  $3^\circ$  (or  $\ell \geq 60$ ), and in regions away from the Galactic plane, the statistics of the 408 MHz map is consistent with the Gaussian sky realisations. Our finding is consistent with the earlier results from Ben-David et al. (2015b), who reported that the Gaussian approximation is valid for scales  $3.7^\circ$  away from the Galactic plane. Unlike binned bispectrum analysis, the MFs results are sensitive to higher order correlations. However, for low sky brightness threshold  $T < 25$  K MFs of the real data agrees well within  $3\sigma$  with the Gaussian simulations. This indicates that for angular scales  $\ell_c \geq 60$ , the actual data is consistent with the Gaussian

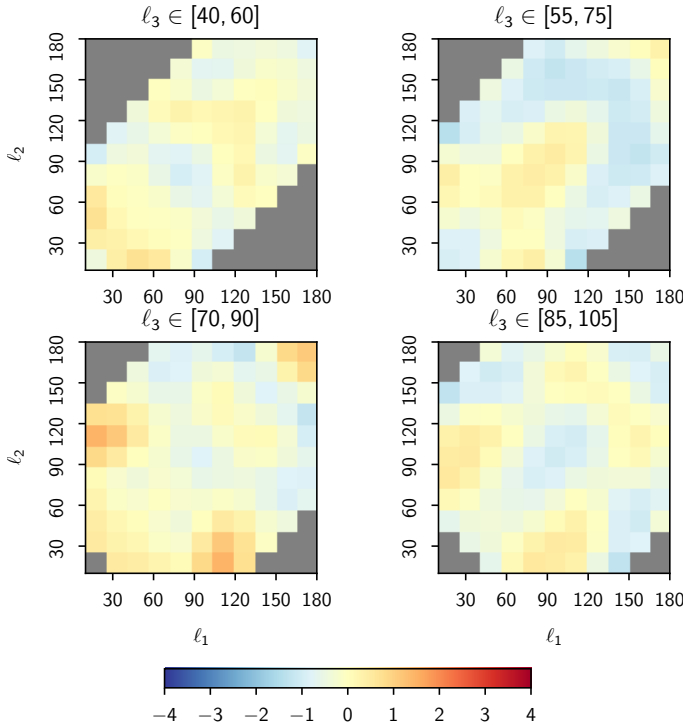


**Figure 6.** Same as Fig. 3, but for 408 MHz sky brightness threshold  $T < 25$  K.

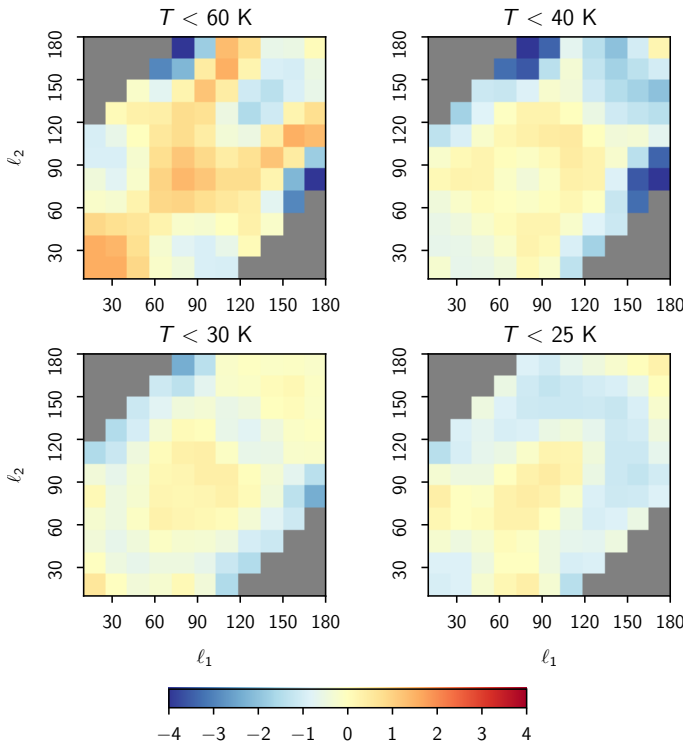


**Figure 7.** Variation of  $\Delta$  plane by fixing  $\ell_3 \in [55, 75]$  for different sky brightness thresholds. It clearly shows decreasing trend of bispectrum signal as we go from high to low  $T$  maps.

simulations. Our study validates the use of Gaussian approximation in Galactic synchrotron simulations, as long as we restrict ourselves to cooler parts of the sky and smaller angular scales.

In near future, we expect to have more of high-resolution full or partial sky coverage low-frequency foreground maps from existing or upcoming next-generation radio telescope facilities. Studying higher order correlation on such maps will help us understand and improve our foreground knowledge for future EOR experiments.

## ACKNOWLEDGEMENT

We acknowledge the use of HPC facility at IISER Mohali. We thank Tarun Souradeep for helpful discussion on bispectrum theory. SR thanks Benjamin Racine and Biuse Casaponsa for helping out with binned bispectrum estimator and code development and testing. The authors acknowledge NISER Bhubaneswar for funding academic visits regarding the project and the use of their HPC facility. This research has made use of NASA Astrophysics Data System Bibliographic Services. Some of the results in this paper have been derived using the HEALPIX (Górski et al. 2005) package.

## APPENDIX A: BINNED STATISTICS

In addition to estimating bispectrum, we also studied higher order statistics such as skewness ( $s$ ), and kurtosis ( $\kappa$ ) of real ( $a_{\ell m}^r$ ) and imaginary ( $a_{\ell m}^i$ ) part of  $a_{\ell m}$  distribution corresponds to different  $i$  bins. We then look how much they differ from each other in case of the actual map, and corresponding Gaussian realisations (see Fig. A1). Both skewness and kurtosis of  $a_{\ell m}$  distribution in the real data are in agreement with corresponding Gaussian realisations. The skewness of  $a_{\ell m}$  is sensitive to the equilateral bispectrum configuration  $\ell_1 \simeq \ell_2 \simeq \ell_3$  (Pietrobon et al. 2009).

## REFERENCES

- Adler R. J., 1981, *The Geometry of Random Fields*
- Ali S. S., Bharadwaj S., Chengalur J. N., 2008, *Monthly Notices of the Royal Astronomical Society*, 385, 2166
- Ben-David A., Liu H., Jackson A. D., 2015a, *Journal of Cosmology and Astroparticle Physics*, 2015, 051
- Ben-David A., von Hausegger S., Jackson A. D., 2015b, *Journal of Cosmology and Astroparticle Physics*, 2015, 019
- Bharadwaj S., Pandey S. K., 2005, *Monthly Notices of the Royal Astronomical Society*, 358, 968
- Bucher M., Van Tent B., Carvalho C. S., 2010, *MNRAS*, 407, 2193
- Bucher M., Benjamin R., Bartjan v. T., 2016, *JCAP*, 2016, 055
- Buchert T., France M. J., Steiner F., 2017, *Classical and Quantum Gravity*, 34, 094002
- Casaponsa B., Barreiro R. B. and Martinez-Gonzalez E., Curto A., Bridges M., Hobson M. P., 2013, *MNRAS*, 434, 796
- Chapman E., Zaroubi S., Abdalla F. B., Dulwich F., Jeli V., Mort B., 2016, *Monthly Notices of the Royal Astronomical Society*, 458, 2928
- Chen G., Szapudi I., 2005, *The Astrophysical Journal*, 635, 743
- Chingangbam P., Park C., 2013, *JCAP*, 2, 031
- Chon G., Challinor A., Prunet S., Hivon E., Szapudi I., 2004, *MNRAS*, 350, 914



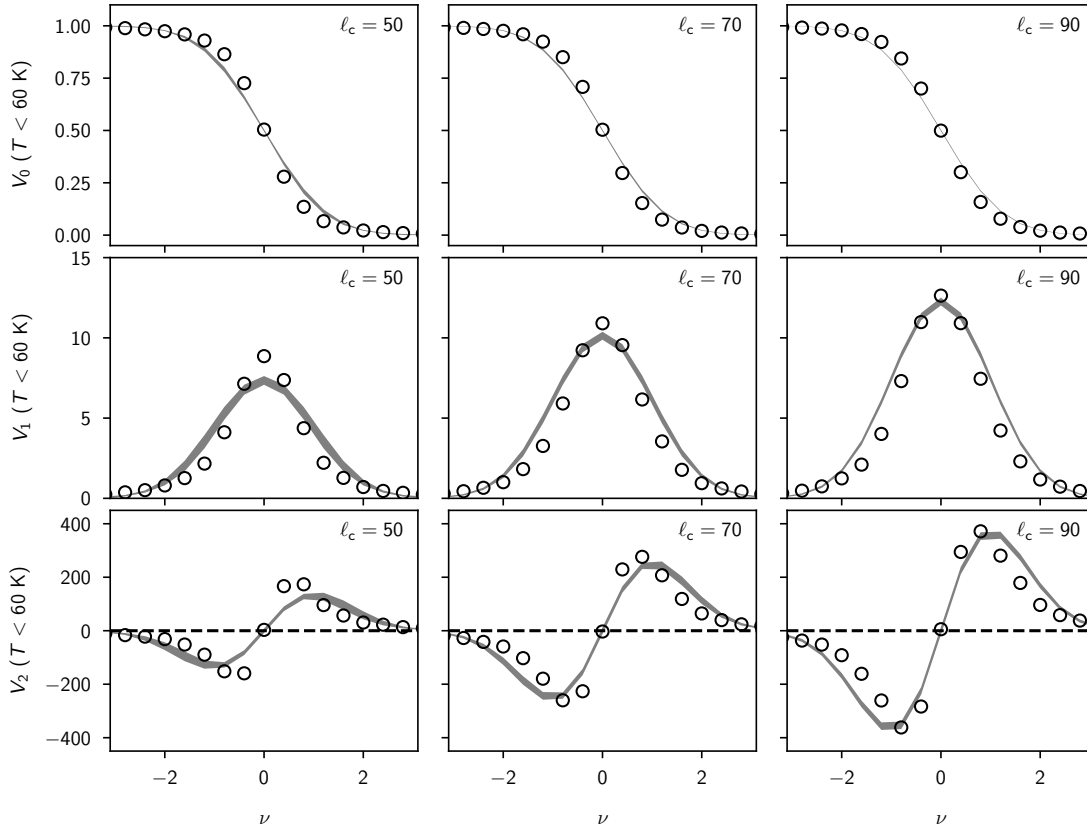


**Figure 8.** Black points indicate the variation of three MF for different cut-off ( $\ell_c$ ) in 408 MHz map with the sky brightness threshold,  $T < 60$  K. Gray shaded region indicates  $3\text{-}\sigma$  deviation from the ensemble mean of 1000 Gaussian realisations.

Choudhuri S., Bharadwaj S., Chatterjee S., Ali S. S., Roy N., Ghosh A., 2016, *Monthly Notices of the Royal Astronomical Society*, 463, 4093

Contaldi C. R., Ferreira P. G., Magueijo J., Grski K. M., 2000, *The Astrophysical Journal*, 534, 25

Cooray A., 2005, *Monthly Notices of the Royal Astronomical Society*, 363, 1049

Datta A., Bowman J. D., Carilli C. L., 2010, *The Astrophysical Journal*, 724, 526

De Oliveira-Costa A., Tegmark M., Gaensler B. M., Jonas J., Landecker T. L., Reich P., 2008, *Monthly Notices of the Royal Astronomical Society*, 388, 247

Ducout A., Bouchet F. R., Colombi S., Pogossyan D., Prunet S., 2013, *MNRAS*, 429, 2104

Fergusson J. R., Liguori M., Shellard E. P. S., 2012, *JCAP*, 12, 032

Furlanetto S. R., Peng Oh S., Briggs F. H., 2006, *Physics Reports*, 433, 181

Gangui A., Martin J., 2000, *Phys. Rev. D*, 62, 103004

Ghosh A., Prasad J., Bharadwaj S., Ali S. S., Chengalur J. N., 2012, *Monthly Notices of the Royal Astronomical Society*, 426, 3295

Giardino G., Banday A. J., Grski K. M. and Bennett K., Jonas J. L., Tauber J., 2002, *AAP*, 387, 82

Górski K. M., Hivon E., Banday A. J., Wandelt B. D., Hansen F. K., Reinecke M., M. B., 2005, *The Astrophysical Journal*, 622, 759

Gott III J. R., Park C., Juszkiewicz R., Bies W. E., Bennett D. P., Bouchet F. R., Stebbins A., 1990, *ApJ*, 352, 1

Harker G., et al., 2009, *MNRAS*, 397, 1138

Haslam C. G. T., Salter C. J. and Stoffel H., Wilson W. E., 1982, *AAP*, 47, 53

Jélic V., Zaroubi S., Labropoulos P., Thomas R. M., Bernardi G., Brentjens M. A., de Bruyn A. G., 2008, *MNRAS*, 389, 1319

Jélic V., Zaroubi S., Labropoulos P., Bernardi G., de Bruyn A. G., Koopmans L. V. E., 2010, *Monthly Notices of the Royal Astronomical Society*, 409, 1647

Komatsu E., Spergel D. N., 2001, *PRD*, 63, 063002

Komatsu E., Spergel D. N., Wandelt B. D., 2005, *ApJ*, 634, 14

Komatsu E., et al., 2011, *ApJS*, 192, 18

Lewis A., Challinor A., Hanson D., 2011, *JCAP*, 3, 018

Liu A., Tegmark M., 2012, *Mon. Not. Roy. Astron. Soc.*, 419, 3491

Liu A., Tegmark M., Bowman J., Hewitt J., Zaldarriaga M., 2009, *Monthly Notices of the Royal Astronomical Society*, 398, 401

Mangilli A., Verde L., 2009, *PRD*, 80, 123007

Mecke K. R., Buchert T., Wagner H., 1994, *AAP*, 288, 697

Morales M. F., Bowman J. D., Hewitt J. N., 2006, *The Astrophysical Journal*, 648, 767

Munshi D., Smidt J., Cooray A., Renzi A., Heavens A., Coles P., 2013, *MNRAS*, 434, 2830

Munshi D., Corasaniti P. S., Coles P., Heavens A., Pandolfi S., 2014, *Monthly Notices of the Royal Astronomical Society*, 442, 3427

Munshi D., Hu B., Matsubara T., Coles P., Heavens A., 2016, *JCAP*, 4, 056

Novikov D., Schmalzing J., Mukhanov V. F., 2000, *AAP*, 364, 17

Pen U. L., Chang T., Peterson J. B., Roy J., Gupta Y., Hirata C. M.,

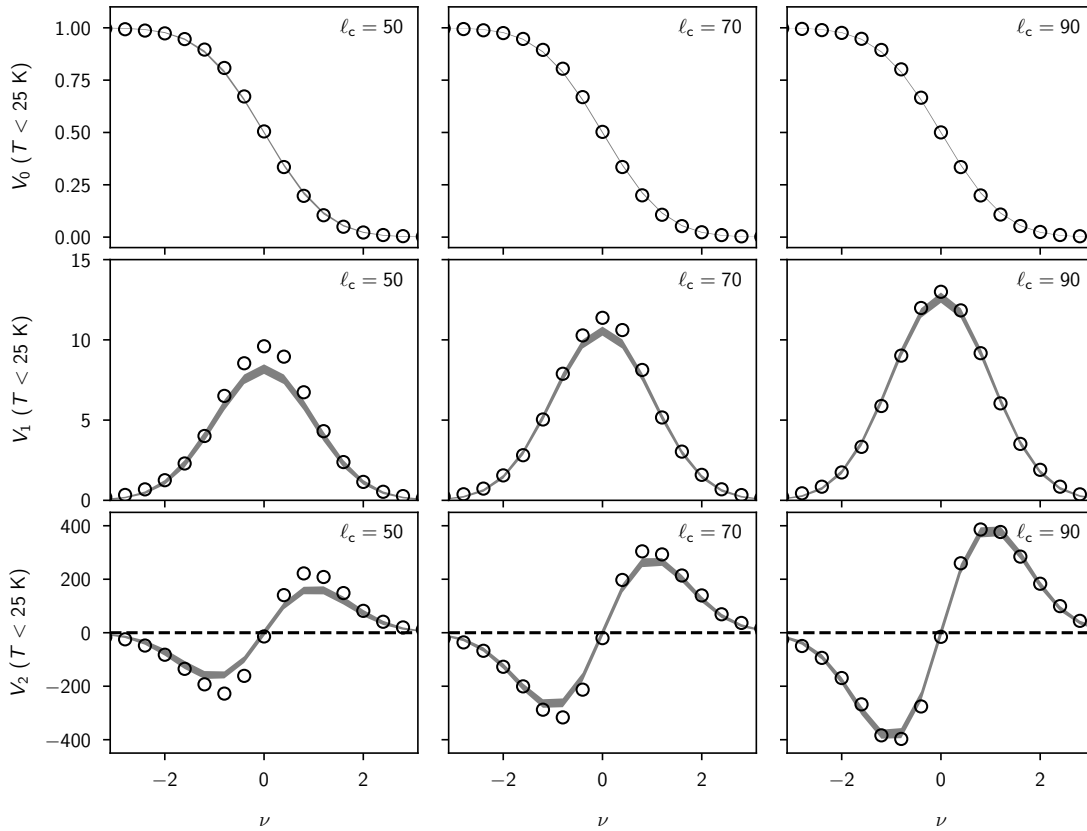


**Figure 9.** Same as Fig. 8, but for 408 MHz brightness threshold  $T < 25$  K. Both the data and Gaussian simulations, agree with each other well within  $3\text{-}\sigma$  for angular scales  $\leq 3^\circ$ .

Odegova J., Sigurdson K., 2009, *Monthly Notices of the Royal Astronomical Society*, 399, 181  
 Pietrobon D., Cabella P., Balbi A., de Gasperis G., Vittorio N., 2009, *MNRAS*, 396, 1682  
 Planck Collaboration et al., 2016, *AAP*, 594, A17  
 Pober J. C., et al., 2013, *ApJL*, 768, L36  
 Remazeilles M., Dickinson C., Banday A. J., Bigot-Sazy M. A., Ghosh T., 2015, *Monthly Notices of the Royal Astronomical Society*, 451, 4311  
 Rogers A. E. E., Bowman J. D., 2008, *The Astronomical Journal*, 136, 641  
 Rotenberg M., Bivens R., Metropolis N., Wooten J. K., 1959, *The 3j and 6j Symbols*. Cambridge, MA: MIT Press  
 Santos M. G., et al., 2003, *Monthly Notices of the Royal Astronomical Society*, 341, 623  
 Santos M. G., Cooray A., Knox L., 2005, *The Astrophysical Journal*, 625, 575  
 Schmalzing J., Buchert T., 1997, *ApJL*, 482, L1  
 Schmalzing J., Gorski K. M., 1998, *MNRAS*, 297, 355  
 Serra P., Cooray A., 2008, *PRD*, 77, 107305  
 Shaver P. A., Windhorst R. A., Madau P., de Bruyn A. G., 1999, *AAP*, 345, 380  
 Shaw J. R., Sigurdson K., Sitwell M., Stebbins A., Pen U.-L., 2015, *PRD*, 91, 083514  
 Subrahmanya C. R., Manoharan P. K., Chengalur J. N., 2017, *Journal of Astrophysics and Astronomy*, 38, 10  
 Tegmark M., Eisenstein D. J., Hu W., de Oliveira-Costa A., 2000, *The Astrophysical Journal*, 530, 133  
 Tingay S. J., Goeke R., Bowman J. D., Emrich D., Ord S. M.,

Mitchell D. A., Morales M. F., 2013, *PASA*, 30, e007  
 Tomita H., 1986, *Progress of Theoretical Physics*, 76, 952  
 Trott C. M., Pindor B., Procopio P., Wayth R. B., Mitchell D. A., McKinley B., Tingay S. J., 2016, *ApJ*, 818, 139  
 Waelkens, A. Jaffe, T. Reinecke, M. Kitaura, F. S. Enlin, T. A. 2009, *AAP*, 495, 697  
 Wang X., Tegmark M., Santos M. G., Knox L., 2006, *The Astrophysical Journal*, 650, 529  
 van Haarlem M. P., Wise M. W., Gunst A. W., Heald G., McKean J. P., Hessels J. W. T., de Bruyn A. G., 2013, *AAP*, 556, A2

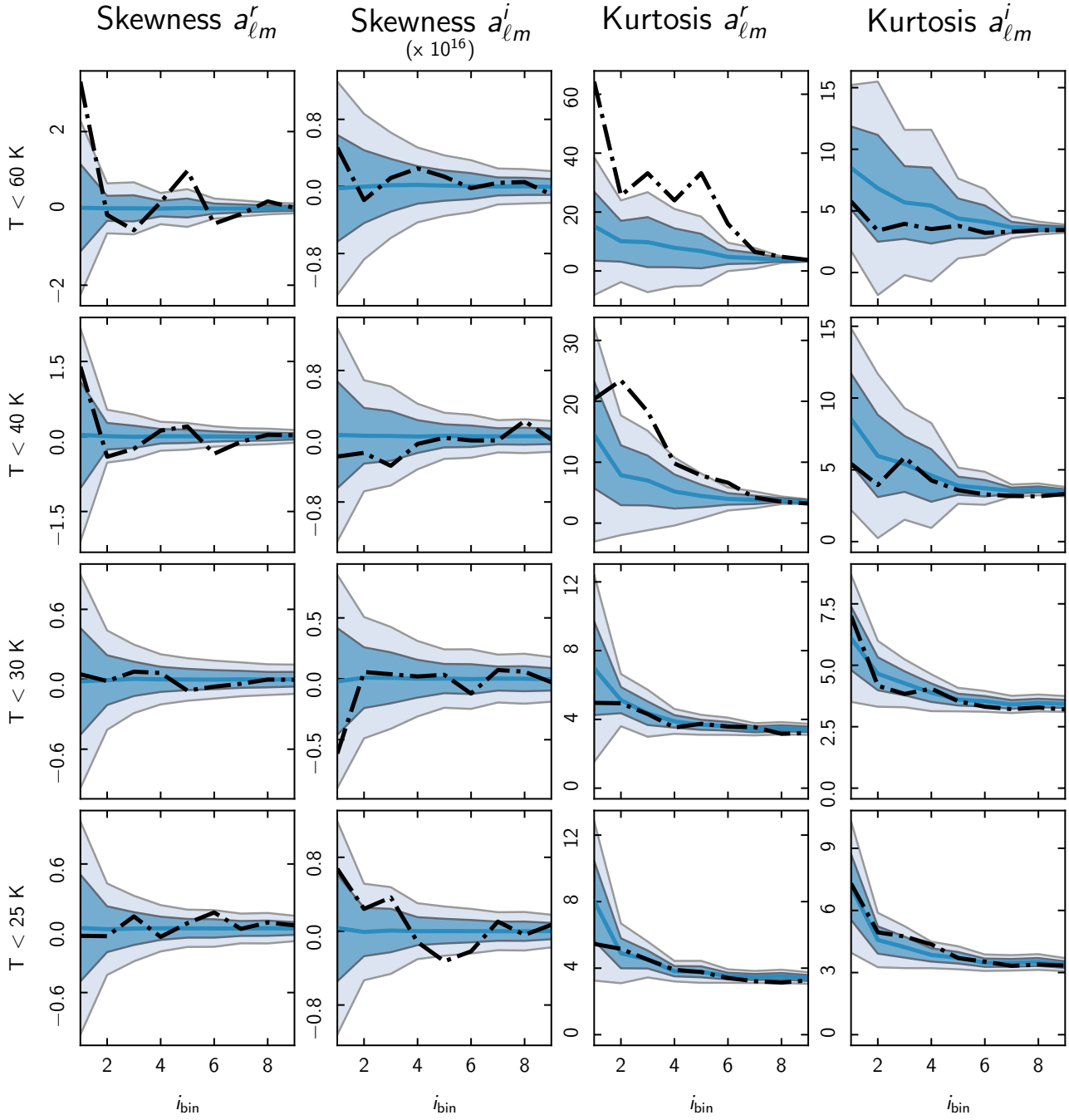


**Figure A1.**  $a_{\ell m}$  skewness and kurtosis versus  $i$  bins: light-blue line is mean value of  $a_{\ell m}$  over 1000 Gaussian realisation in  $i$  bin and shaded regions are  $1\sigma$  and  $2\sigma$  confidence regions, black dashed line corresponds to actual map  $a_{\ell m}$  value in  $i_{bin}$ .